

# A global resource allocation strategy governs growth transition kinetics of *Escherichia coli*

David W. Erickson<sup>1\*</sup>, Severin J. Schink<sup>1,2\*</sup>, Vadim Patsalo<sup>3</sup>, James R. Williamson<sup>3</sup>, Ulrich Gerland<sup>2</sup> & Terence Hwa<sup>1</sup>

**A grand challenge of systems biology is to predict the kinetic responses of living systems to perturbations starting from the underlying molecular interactions. Changes in the nutrient environment have long been used to study regulation and adaptation phenomena in microorganisms<sup>1–3</sup> and they remain a topic of active investigation<sup>4–11</sup>. Although much is known about the molecular interactions that govern the regulation of key metabolic processes in response to applied perturbations<sup>12–17</sup>, they are insufficiently quantified for predictive bottom-up modelling. Here we develop a top-down approach, expanding the recently established coarse-grained proteome allocation models<sup>15,18–20</sup> from steady-state growth into the kinetic regime. Using only qualitative knowledge of the underlying regulatory processes and imposing the condition of flux balance, we derive a quantitative model of bacterial growth transitions that is independent of inaccessible kinetic parameters. The resulting flux-controlled regulation model accurately predicts the time course of gene expression and biomass accumulation in response to carbon upshifts and downshifts (for example, diauxic shifts) without adjustable parameters. As predicted by the model and validated by quantitative proteomics, cells exhibit suboptimal recovery kinetics in response to nutrient shifts owing to a rigid strategy of protein synthesis allocation, which is not directed towards alleviating specific metabolic bottlenecks. Our approach does not rely on kinetic parameters, and therefore points to a theoretical framework for describing a broad range of such kinetic processes without detailed knowledge of the underlying biochemical reactions.**

We focus on growth transitions between carbon substrates that can be co-utilized<sup>21</sup> or those that are closely related and hence readily switchable, avoiding prolonged growth arrests or heterogeneous growth characteristics<sup>8,9,11</sup> for which even the steady-state behaviours are poorly characterized. We first studied nutrient upshifts by growing a wild-type *Escherichia coli* K-12 strain (NCM3722) in minimal medium, with succinate as the sole carbon substrate. During exponential growth, a second, co-utilized carbon substrate<sup>21</sup> (gluconate) was added (Fig. 1 and Methods). The time course of optical density at 600 nm ( $OD_{600\text{ nm}}$ ) of the cell culture (a proxy for cell mass  $M$ , Extended Data Fig. 1a), was measured throughout the transition (Fig. 1a); faster growth occurred soon after the shift. Ribosome content (reported by RNA abundance<sup>16</sup>) increased faster than cell mass, as is well known<sup>3</sup>, whereas catabolic protein content (reported by LacZ expression induced in medium with isopropyl  $\beta$ -D-1-thiogalactopyranoside, IPTG<sup>15</sup>) took several hours to adapt. Eventually, all these quantities grew at the same rate, as is required for balanced growth. The instantaneous growth rate,  $\lambda \equiv \text{dln}M/\text{d}t$ , slowly converged to its final value  $\lambda_f$  over the course of several hours (Fig. 1b, and Extended Data Fig. 2a for longer times). Biomass synthesis flux,  $J \equiv \text{d}M/\text{d}t$ , responded rapidly: the final rate of increase was reached within 30 min of the upshift (Fig. 1c). A similar fast response is observed for the synthesis of new RNA and LacZ

(Fig. 1d, e), with expression levels (slope of the data) approaching the final value (slope of the dashed lines) within one mass-doubling after the upshift.

Next, we characterized the kinetics of nutrient downshifts, resulting from the depletion of a nutrient component in the medium as in Monod's study of diauxic growth<sup>1</sup>. Wild-type cells were grown on saturating amounts of succinate and small amounts of glucose (Fig. 1f): as glucose is co-utilized with succinate<sup>21</sup>, cells first used both carbon substrates and switched to succinate-only after glucose was depleted. At this point, the instantaneous growth rate  $\lambda(t)$  decreased sharply (Fig. 1g). During the recovery, RNA and LacZ (Fig. 1i, j) showed decreased and increased expression levels (slope of the data), respectively, eventually settling to the final level (slope of the dashed lines). Both the upshift and the downshift are highly repeatable (Extended Data Fig. 2b) and similar behaviour has been observed for eight other substrate pairs for upshifts (Extended Data Fig. 3) and four other substrate pairs for downshifts (Extended Data Fig. 4), covering a wide range of initial and final growth rate combinations.

The recovery processes shown in Fig. 1 are controlled by regulatory interactions. Despite an abundance of molecular knowledge, particularly regarding the regulation of ribosome synthesis by guanosine tetraphosphate (ppGpp)<sup>13,14,16,17</sup> and the regulation of carbon catabolism by the cAMP–cAMP receptor protein (cAMP–CRP) signalling system<sup>12,15</sup>, quantitative characterization of the dynamics of these regulatory processes is lacking. Models that do not include the dynamics of gene regulation are incapable of consistently describing the different types of recovery kinetics after different nutrient shifts (Supplementary Note 1 and Extended Data Fig. 5). Here we introduce a coarse-grained kinetic model that quantitatively incorporates the regulation of catabolism and protein synthesis, despite the lack of kinetic parameters describing the molecular processes. We assume that the kinetics of growth recovery is limited by the abundances of a number of key internal metabolites, including ketoacids and amino acids<sup>11,22</sup>, which we coarse-grain into a single pool of 'central precursors', as these metabolites are connected by rapid reversible reactions<sup>23</sup>. As illustrated in Fig. 2, this precursor pool is filled by carbon influx  $J_C$  (equation (1) in Fig. 2) and depleted by ribosomes during protein synthesis. Because the translational activity of the ribosomes,  $\sigma(t)$ , defined mathematically as the average translation rate<sup>24</sup>, is set by the precursor pool, we assume it adjusts on a coarse-grained time scale such that the flux of protein synthesis  $J_R$  balances the carbon influx  $J_C$  (equations (2a) and (2b) in Fig. 2).

The allocation of protein synthesis is dictated by gene-regulatory functions: an increase in the precursor pool upregulates the synthesis of ribosomes (blue, equation (3a) in Fig. 2) via the function  $\chi_{\text{Rb}}(t)$ , which is controlled by ppGpp signalling<sup>13,14,16,17</sup>. Concomitantly, the synthesis of catabolic proteins (green, equation (4a) in Fig. 2) is repressed via  $\chi_{\text{Cat}}(t)$  and controlled by the cAMP–CRP signalling system<sup>12,15</sup>. Hence both regulatory functions depend on the precursor

<sup>1</sup>Department of Physics, University of California San Diego, La Jolla, California 92093, USA. <sup>2</sup>Physics of Complex Biosystems, Physics Department, Technical University of Munich, 85748 Garching, Germany. <sup>3</sup>Department of Integrative Structural and Computational Biology, Department of Chemistry, The Skaggs Institute for Chemical Biology, The Scripps Research Institute, La Jolla, California 92037, USA.

\*These authors contributed equally to this work.

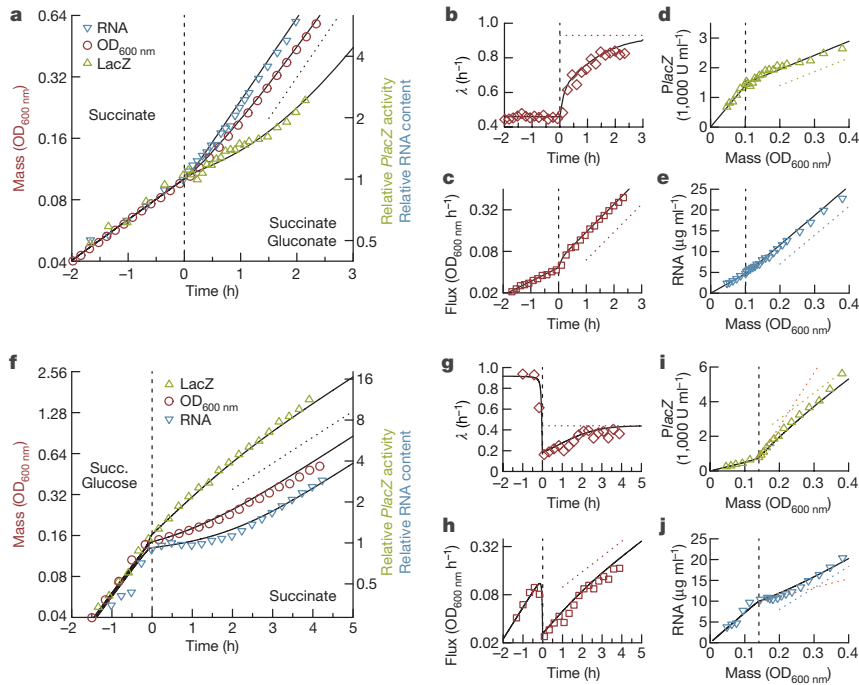


**Figure 1 | Nutrient up- and downshifts.** *E. coli* K-12 grown in minimal medium (and IPTG to induce LacZ) are shifted by the addition of a second nutrient or by the depletion of a nutrient. **a–e**, Upshift upon addition of a second nutrient: 20 mM succinate (present continuously), 20 mM gluconate (present only after  $t = 0$ ). **f–j** Downshift upon depletion of a nutrient: 20 mM succinate (present continuously), 0.03% glucose (depleted around  $t = 0$ ). **a, f**, Optical density ( $OD_{600\text{ nm}}$ , red circles), RNA abundance (RNA amount per culture volume, blue inverted triangles), and LacZ activity per culture volume, both relative to  $t = 0$  (green triangles), are plotted versus time. The slope of the dotted line indicates final growth rates (upshift,  $\lambda_f = 0.98\text{ h}^{-1}$ ; downshift,

$\lambda_f = 0.45\text{ h}^{-1}$ ). **b, g**, Instantaneous growth rate  $\lambda(t)$  (red diamonds). Red dotted lines indicate  $\lambda_f$ . **c, h**, Time derivative of  $OD_{600\text{ nm}}$  (biomass flux, red squares). The slope of the dotted line indicates  $\lambda_f$ . **d, e, i, j**, Absolute LacZ activity and RNA abundance plotted versus  $OD_{600\text{ nm}}$ . The slopes of the green and blue lines indicate final expression levels (defined in fractions of the total protein, see Supplementary equation (8) in Supplementary Note 2); the slopes of the orange lines indicate predicted expression levels immediately after the shift. The data are highly repeatable, see Extended Data Fig. 2. In all panels, the black curves are fit-parameter-free predictions of the FCR model, obtained as outlined in Methods.

pool, which also sets the translational activity  $\sigma$ . These observations led us to formulate our key approach, which closes the model equations and renders them independent of molecular details: we use the translational activity  $\sigma(t)$  to set the regulatory functions  $\chi_{Rb}(t)$  and  $\chi_{Cat}(t)$

via the steady state relations,  $\hat{\chi}_{Rb}(\sigma)$  and  $\hat{\chi}_{Cat}(\sigma)$ . The latter are shown in Fig. 2b and are obtained from the previously characterized ‘growth laws’<sup>15,18</sup> (Extended Data Fig. 1c–g). This is stated explicitly in equations (3b) and (4b) in Fig. 2 and amounts to a quasi-steady state assumption

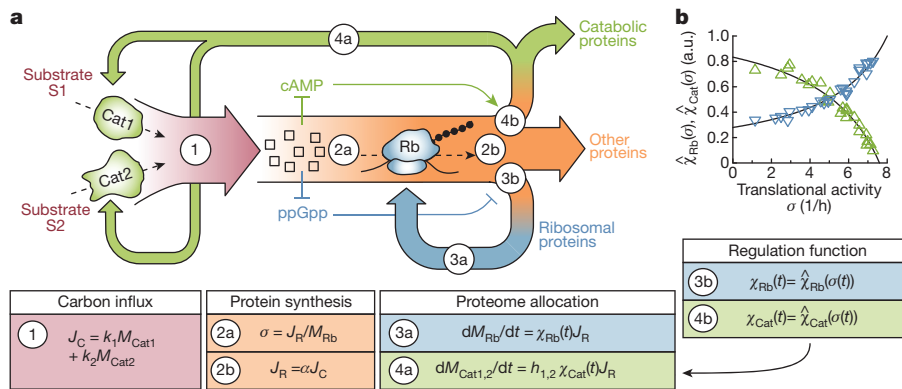


**Figure 2 | Model of FCR.** **a**, Flux balance and allocation of protein synthesis. Carbon substrates S1 and S2 are imported by uptake proteins Cat1 and Cat2 of abundances  $M_{Cat1}$  and  $M_{Cat2}$  at rates  $k_1$  and  $k_2$ , respectively. Changes in the external concentrations of these substrates result in changes in the carbon influx  $J_C$  (red, equation (1)), which supplies a pool of central precursors (squares). These precursors are consumed by the ribosomes (Rb) for protein synthesis, the flux of which  $J_R$  (orange, equation (2b)), with  $\alpha$  being a conversion factor from carbon to protein) must balance the changes in the carbon influx at a coarse-grained timescale. Attaining this protein synthesis flux for a given number of ribosomes (of abundance  $M_{Rb}$ ) requires changes in the translational activity  $\sigma$  as defined in equation (2a). Molecularly, changes in  $\sigma$  are attributed to changes in the precursor pool<sup>16,24</sup>. Parts of the protein

synthesis flux are allocated to the expression of catabolic and ribosomal proteins,  $M_{Rb}$  and  $M_{Cat1,2}$  (equations (3a) and (4a)). This allocation is determined by the global regulation functions  $\chi_{Rb}(t)$  and  $\chi_{Cat}(t)$ , set molecularly by the precursor pool via ppGpp (blue arrows)<sup>13,16</sup> and the cAMP–CRP system (green arrows)<sup>15</sup>, respectively, as well as the substrate-specific regulation  $h_{1,2}$  (Supplementary Note 3). **b**, The forms of the regulatory functions  $\hat{\chi}_{Rb}(\sigma)$  and  $\hat{\chi}_{Cat}(\sigma)$  (black lines) can be determined from the known steady-state measurements (Extended Data Fig. 1c, d) as derived in Supplementary Note 2.2d–f. The central simplifying assumption of the model is that the time-dependence of the regulation functions during growth transition is determined solely through the changes in  $\sigma$ , as expressed explicitly in equations (3b) and (4b).

(Supplementary Notes 3 and 4). By construction, the resulting coarse-grained model does not attempt to address very rapid kinetic processes, for example, ribosomal oscillation during upshift to rich medium<sup>25</sup>. However, it describes the kinetics of cell growth and gene expression on slower timescales, for example, from around ten minutes until the attainment of the new steady state, provided that the growth transitions do not involve prolonged periods of growth arrest<sup>8</sup>, which would invalidate the quasi-steady-state approximation.

We refer to this model of gene regulation as flux-controlled regulation (FCR), because the key dynamic variable  $\sigma(t)$ , which controls gene expression via the regulatory functions  $\chi_{Rb}$  and  $\chi_{Cat}$  (equations (3a) and (4a) in Fig. 2), is set by the condition of flux balance (equations (2a) and (2b) in Fig. 2). Combining all the equations shown in Fig. 2 (detailed in Supplementary Note 4.1), we obtain a single nonlinear differential equation describing the kinetics after the shift ( $t > 0$ ):

$$\frac{d\sigma}{dt} = \sigma(t) \cdot [\mu_f \hat{\chi}_{Cat}(\sigma(t)) - \sigma(t) \hat{\chi}_{Rb}(\sigma(t))], \quad (5)$$

where  $\hat{\chi}_{Cat}$  and  $\hat{\chi}_{Rb}$  are the regulatory functions given in Fig. 2b. equation (5) can be solved analytically (Supplementary Note 4.2). The timescale of this logistic-like equation is set by the rate  $\mu_f$ , which characterizes the maximal carbon uptake rate in the post-shift medium; its value can be fixed through its relation with the steady-state growth rate  $\lambda_f$  in the post-shift medium,  $\mu_f \equiv \lambda_f / (1 - \lambda_f / \lambda_C)$ , where  $\lambda_C = 1.17 \text{ h}^{-1}$  is a known, strain-specific constant of the growth laws (Extended Data Fig. 1d and Supplementary Note 2.3). The time courses of mass  $M(t)$ , ribosomes  $M_{Rb}(t)$ , and all other quantities introduced in Fig. 2 can be obtained analytically from the FCR model (Supplementary Note 4.4 and Methods). For many macroscopic observables, a second timescale set by  $\lambda_f$  emerges after the dynamics of equation (5) have relaxed, due to slow growth-mediated dilution of the inherited proteome.

The solution also requires the specification of the initial condition  $\sigma(0)$ , the translational activity directly after a shift. For upshifts, this depends on the abundance of the uptake system Cat2 (for the newly added substrate) at the time of the upshift, as a sudden increase in carbon influx due to pre-expressed Cat2 leads to an abrupt increase in  $\sigma(0)$ . Many uptake systems are not expressed in the absence of their cognate substrates, so that biomass flux  $J(t)$  and  $\sigma(t)$  are continuous, and the solution of equation (5) is able to describe the entire upshift kinetics without any adjustable parameters (Fig. 1a–e and Extended Data Fig. 3, black panels).

In some instances, we observe an abrupt jump in biosynthesis flux  $J(t)$  at the instant of upshift (see, for example, Extended Data Fig. 6), possibly owing to the expression of Cat2 during pre-shift growth. Such pre-expression can be accommodated in the FCR model by changing the initial condition  $\sigma(0)$  (Extended Data Fig. 6, black lines). By synthetically pre-expressing Cat2 during pre-shift growth, the magnitude of the abrupt jump of flux  $J(t)$  at the moment of the shift can be systematically varied, even to the extent at which the instantaneous growth rate transiently overshoots that of the post-shift state (Extended Data Fig. 7a, b). For these cases, the FCR model quantitatively predicts the magnitude of the flux jump, as verified in Extended Data Fig. 7d.

The same FCR model quantitatively captures the very different dynamics of downshifts between co-utilized carbon substrates (Fig. 1f–j and Extended Data Fig. 4, black lines). Here, Monod kinetics with established Michaelis constants were used to model carbon substrate depletion (Supplementary Note 4.2a), again without adjustable parameters. The magnitude of the drop of flux and growth rate after substrate depletion is determined by the expression level of Cat2, which is downregulated during growth on both substrates compared to substrate S2 only (Supplementary Note 4.2d and Supplementary equation (57)). The FCR model was further expanded to capture the growth shift between hierarchically used carbon substrates, specifically the paradigmatic glucose–lactose diauxie<sup>1</sup> (Fig. 3). Here, inducer exclusion<sup>26</sup>

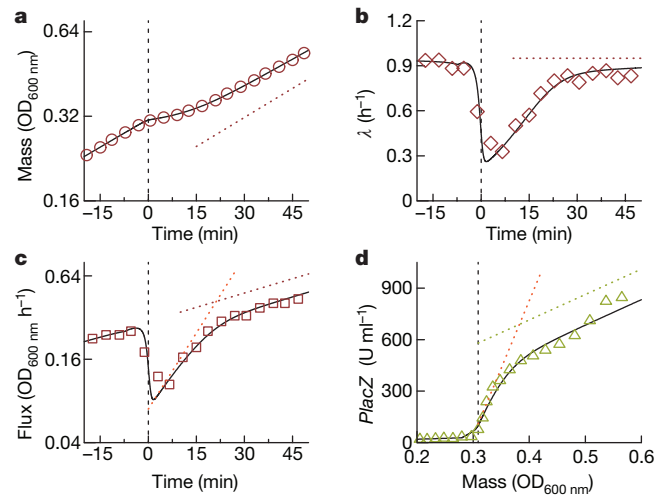


**Figure 3 | Diauxic shift between hierarchically used carbon substrates.**

**a**, *E. coli* K-12 grown on 0.03% glucose and 0.2% lactose. Initially, only glucose is used<sup>1</sup>. Around time  $t = 0$  glucose was depleted and lactose uptake and metabolism were activated. The dotted red line indicates the growth rate on lactose only,  $\lambda_f = 0.95 \text{ h}^{-1}$ . **b**, The instantaneous growth rate  $\lambda(t)$  dropped abruptly after glucose depletion, followed by a rapid recovery to  $\lambda_f$  (dotted horizontal line). **c**, After glucose depletion, biomass flux increased at an increased rate, before settling to the final rate. The slope of the red dotted line indicates  $\lambda_f$ , the slope of the orange dotted line indicates  $\mu_f$ . **d**, Lactose catabolic enzyme LacZ (green triangles) is tightly repressed before the shift ( $98 \text{ U ml}^{-1}$  at  $\text{OD}_{600 \text{ nm}}$ ), then increases rapidly after the shift, before settling at the final expression level indicated by the slope of the green dotted line ( $1,557 \text{ U ml}^{-1}$  at  $\text{OD}_{600 \text{ nm}}$ , obtained from steady-state growth in lactose only). The dotted orange line, with slope  $\mu_f \lambda_f \times 1,557 \text{ U ml}^{-1} \text{ OD}_{600 \text{ nm}} = 7,866 \text{ U ml}^{-1} \text{ OD}_{600 \text{ nm}}$ , is the predicted response immediately after shift according to Supplementary equation (18) of Supplementary Note 2. The black curves are full predictions of the FCR theory using the timepoint of *lac* operon activation as the single fitting parameter (see Supplementary Note 3.2g).

prevents the uptake of lactose and the expression of the *lac* operon as long as glucose is present and taken up. Without invoking the details of how precisely inducer exclusion is removed, we introduced the switch-on time of the *lac* operon as the lone fitting parameter (Supplementary Note 3.2g) and find that the FCR model accurately describes the glucose–lactose diauxie also (Fig. 3, black lines).

The quantitative agreement of the model output with the measured observables is remarkable, given the simplicity of the model, and especially the lack of free parameters. As discussed in Extended Data Fig. 8, upshifts and downshifts show different recovery kinetics, despite being controlled by the same underlying regulatory strategy. In upshifts, the reallocation of protein synthesis quickly settles (Extended Data Fig. 8a, dashed lines), and recovery is dominated by growth-mediated relaxation of the abundances of catabolic proteins and ribosomes towards their final states. In downshifts, the phase of active reallocation of protein synthesis spans the entire recovery (Extended Data Fig. 8b, dashed lines). Owing to their different adaptation, upshifts are dominated by the timescale  $\lambda_f^{-1}$ , whereas downshifts are dominated by  $\mu_f^{-1}$  (Supplementary Note 6 and Extended Data Fig. 9), explaining why the diauxic shift of Fig. 3 ( $\mu_f = 5.1 \text{ h}^{-1}$ ) relaxes fivefold faster than the upshift of Fig. 1 ( $\lambda_f = 0.98 \text{ h}^{-1}$ ). In both shifts, the regulatory functions do not slide along the steady-state lines, despite being derived from them (Supplementary Note 2; compare the black and the coloured lines in Extended Data Fig. 8c).

The complete recovery after nutrient shifts is surprisingly slow, considering that the number of desired proteins needed to overcome the metabolic bottleneck is small; for example, Cat2 for upshift and Cat1 for downshift comprise no more than a few per cent of the entire proteome. They should thus take only a few per cent of the doubling

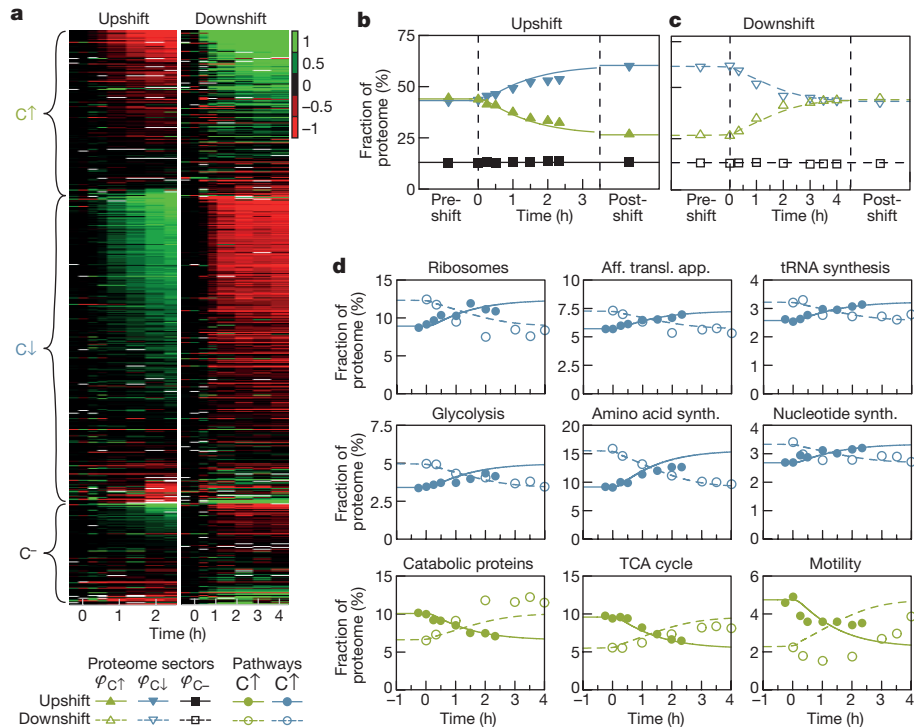


**Figure 4 | Proteome composition during recovery.** **a**, Expression of individual proteins during the up- and downshift of Fig. 1, relative to the pre-shift steady state (colour scale: log<sub>2</sub>). Proteins are grouped according to their steady-state response (see Methods) to decreasing growth rate by carbon limitation:  $C^\uparrow$  (increase; green),  $C^\downarrow$  (decrease; blue) and  $C^-$  (no response; black)<sup>19</sup>. **b**, **c**, Absolute proteome fractions of the protein sectors  $\varphi_{C^\uparrow}$ ,  $\varphi_{C^\downarrow}$  and  $\varphi_{C^-}$  (symbols) and fit-parameter-free prediction (lines), derived under the assumption that all proteins in sectors  $C^\uparrow$ ,  $C^\downarrow$

time to synthesize, if cells direct protein synthesis exclusively to the limited number of bottleneck proteins, as proposed by recent theories of optimal growth transition strategies<sup>27,28</sup>. Instead, according to the FCR model, cells adopt a regulatory strategy featuring coordinated global remodelling of the proteome well beyond the adjustment of a few specific proteins, but including, for example, a large number of anabolic and catabolic proteins unrelated to the specific sugars in the medium. Indeed, the FCR model makes quantitative predictions for the proteome remodelling dynamics: classifying the proteome according to the steady-state response under carbon limitation<sup>19</sup>, we group proteins increasing, decreasing or not changing under carbon limitation by  $C^\uparrow$ ,  $C^\downarrow$ , and  $C^-$  ‘sectors’, respectively. Because catabolic proteins belong to  $C^\uparrow$  and ribosomes belong to  $C^\downarrow$ <sup>19</sup>, the dynamics of these proteome sectors, allocated by the regulatory functions  $\chi_{C^\uparrow}$  and  $\chi_{C^\downarrow}$ , are specified in the FCR model by the regulatory functions  $\chi_{Cat}(t)$  and  $\chi_{Rb}(t)$  according to the relation equations (6a) and (6b) in Extended Data Fig. 8d, with all constants fixed by the steady-state proteome partitioning (Supplementary Note 5). The dynamics of the sectors  $C^\uparrow$  and  $C^\downarrow$ , manifested by changes in the total mass fractions of all proteins in these sectors denoted by  $\varphi_{C^\uparrow}(t)$  and  $\varphi_{C^\downarrow}(t)$ , are then prescribed by equations (7a) and (7b), shown in Extended Data Fig. 8d. The resulting sector dynamics for upshifts and downshifts are qualitatively sketched in Extended Data Fig. 8e and f, respectively.

We tested these predictions by extending the quantitative mass spectrometry approach<sup>19</sup> to the kinetic regime. Figure 3a shows the time-dependent changes in the abundance of hundreds of proteins during the up- and downshifts presented in Fig. 1. We observe that the dynamic response of the proteins is in line with their steady-state categorization: after a carbon downshift,  $C^\uparrow$  proteins increased (green) and  $C^\downarrow$  proteins decreased (red), whereas the opposite occurred in upshift. The majority of  $C^-$  proteins showed little to no response to

and  $C^-$  follow simple rules of global allocation (Extended Data Fig. 9 and Supplementary Note 5). **d**, Mass fraction of individual pathways or protein groups during upshift (solid lines and symbols) and downshift (dashed lines and open symbols). Colours denote sector affiliation. All biosynthetic pathways follow the theoretical prediction assuming co-regulation. Motility expression (bottom right) is a clear exception, showing a 2 h delay increase during recovery from downshifts, when compared to the expected increase in expression (dashed line). TCA, tricarboxylic acid.

nutrient shifts. The change of protein abundance is dominated by protein expression and growth-mediated dilution, as degradation plays a negligible role during the transition (Extended Data Fig. 10). We estimated the total abundances of proteins belonging to each of these three sectors (see Methods), and plotted their time dependences following up- and downshift (Fig. 4b, c). Their dynamics closely follow the model predictions (lines) throughout the transitions. The same approach was applied to characterize the total abundances of proteins belonging to various major metabolic pathways or functional groups (Fig. 4d and Methods). The dynamics of these groups in upshifts and downshifts largely followed the model predictions too, except for motility proteins, which clearly exhibited a delay under nutrient downshift.

The quantitative matches of the model predictions with the proteome data without adjustable parameters suggest that much of the proteome is indeed co-regulated, governed by a single dynamic control variable as assumed in the model throughout the growth shifts. In our model, this dynamic variable is the translational activity  $\sigma(t)$ , which is itself a proxy for the central metabolite pool (for example the ketoacids and amino acids) as illustrated in Fig. 2a. Because, molecularly, the control is exerted via the messengers cAMP<sup>12,15</sup> and ppGpp<sup>13,14,16,17</sup>, our results suggest that these two signalling pathways are tightly coupled via the central metabolite pool<sup>15,22</sup>, which is the proposed driver of global regulatory control. Notably, even pathways not known to be directly regulated by cAMP or ppGpp, for example amino acid synthesis, are seen to follow the predicted global response following carbon shifts, possibly due to competition for transcriptional or translational resources<sup>16,17</sup>.

Despite the central regulatory roles of these signals, the growth transition kinetics are not sensitive to the kinetic details of these signalling pathways, as evidenced by the predictive power of the FCR model that

does not explicitly include signalling. Rather, the kinetics are governed by the slower timescales of global reallocation of protein synthesis and growth-mediated dilution. The observed resource-allocation strategy maintains global coordination of the proteome, instead of sequentially prioritizing the expression of various bottlenecks<sup>27,28</sup>. This conservative control strategy may be more robust by confining the metabolic bottleneck to the central precursors, which drive global regulatory control (Fig. 2a). Quantitative understanding of proteome-remodelling kinetics is a prerequisite for predicting cellular dynamics, such as the dynamics of genetic circuits or growth in response to stresses, making the framework established here foundational in understanding a broad spectrum of other kinetic phenomena.

**Online Content** Methods, along with any additional Extended Data display items and Source Data, are available in the online version of the paper; references unique to these sections appear only in the online paper.

**Received 22 May 2016; accepted 20 September 2017.**

**Published online 25 October 2017.**

- Monod, J. The phenomenon of enzymatic adaptation and its bearings on problems of genetics and cellular differentiation. *Growth* **11**, 223–289 (1947).
- Kjeldgaard, N. O., Maaløe, O. & Schaechter, M. The transition between different physiological states during balanced growth of *Salmonella typhimurium*. *J. Gen. Microbiol.* **19**, 607–616 (1958).
- Dennis, P. P. & Bremer, H. Regulation of ribonucleic acid synthesis in *Escherichia coli*: An analysis of a shift-up. *J. Mol. Biol.* **75**, 145–159 (1973).
- Thattai, M. & Shraiman, B. I. Metabolic switching in the sugar phosphotransferase system of *Escherichia coli*. *Biophys. J.* **85**, 744–754 (2003).
- Kussell, E. & Leibler, S. Phenotypic diversity, population growth, and information in fluctuating environments. *Science* **309**, 2075–2078 (2005).
- Acar, M., Mettetal, J. T. & van Oudenaarden, A. Stochastic switching as a survival strategy in fluctuating environments. *Nat. Genet.* **40**, 471–475 (2008).
- Boulineau, S. *et al.* Single-cell dynamics reveals sustained growth during diauxic shifts. *PLoS One* **8**, e61686 (2013).
- Kotte, O., Volkmer, B., Radzikowski, J. L. & Heinemann, M. Phenotypic bistability in *Escherichia coli*'s central carbon metabolism. *Mol. Syst. Biol.* **10**, 736 (2014).
- van Heerden, J. H. *et al.* Lost in transition: start-up of glycolysis yields subpopulations of nongrowing cells. *Science* **343**, 1245114 (2014).
- Venturelli, O. S., Zuleta, I., Murray, R. M. & El-Samad, H. Population diversification in a yeast metabolic program promotes anticipation of environmental shifts. *PLoS Biol.* **13**, e1002042 (2015).
- Link, H., Fuhrer, T., Gerosa, L., Zamboni, N. & Sauer, U. Real-time metabolome profiling of the metabolic switch between starvation and growth. *Nat. Methods* **12**, 1091–1097 (2015).
- Kolb, A., Busby, S., Buc, H., Garges, S. & Adhya, S. Transcriptional regulation by cAMP and its receptor protein. *Annu. Rev. Biochem.* **62**, 749–795 (1993).
- Potrykus, K. & Cashel, M. (p)ppGpp: still magical? *Annu. Rev. Microbiol.* **62**, 35–51 (2008).
- Lemke, J. J. *et al.* Direct regulation of *Escherichia coli* ribosomal protein promoters by the transcription factors ppGpp and DksA. *Proc. Natl Acad. Sci. USA* **108**, 5712–5717 (2011).
- You, C. *et al.* Coordination of bacterial proteome with metabolism by cyclic AMP signalling. *Nature* **500**, 301–306 (2013).
- Scott, M., Klumpp, S., Mateescu, E. M. & Hwa, T. Emergence of robust growth laws from optimal regulation of ribosome synthesis. *Mol. Syst. Biol.* **10**, 747 (2014).
- Haurlyuk, V., Atkinson, G. C., Murakami, K. S., Tenson, T. & Gerdes, K. Recent functional insights into the role of (p)ppGpp in bacterial physiology. *Nat. Rev. Microbiol.* **13**, 298–309 (2015).
- Scott, M., Gunderson, C. W., Mateescu, E. M., Zhang, Z. & Hwa, T. Interdependence of cell growth and gene expression: origins and consequences. *Science* **330**, 1099–1102 (2010).
- Hui, S. *et al.* Quantitative proteomic analysis reveals a simple strategy of global resource allocation in bacteria. *Mol. Syst. Biol.* **11**, 784 (2015).
- Basan, M. *et al.* Overflow metabolism in *Escherichia coli* results from efficient proteome allocation. *Nature* **528**, 99–104 (2015).
- Hermesen, R., Okano, H., You, C., Werner, N. & Hwa, T. A growth-rate composition formula for the growth of *E. coli* on co-utilized carbon substrates. *Mol. Syst. Biol.* **11**, 801 (2015).
- Chubukov, V., Gerosa, L., Kochanowski, K. & Sauer, U. Coordination of microbial metabolism. *Nat. Rev. Microbiol.* **12**, 327–340 (2014).
- Reitzer, L. Nitrogen assimilation and global regulation in *Escherichia coli*. *Annu. Rev. Microbiol.* **57**, 155–176 (2003).
- Dai, X. *et al.* Reduction of translating ribosomes enables *Escherichia coli* to maintain elongation rates during slow growth. *Nat. Microbiol.* **2**, 16231 (2016).
- Gausing, K. *Ribosomes: Structure, Function and Genetics* 693–718 (Univ. Park Press, 1980).
- Postma, P. W., Lengeler, J. W. & Jacobson, G. R. Phosphoenolpyruvate: carbohydrate phosphotransferase systems of bacteria. *Microbiol. Rev.* **57**, 543–594 (1993).
- Pavlov, M. Y. & Ehrenberg, M. Optimal control of gene expression for fast proteome adaptation to environmental change. *Proc. Natl Acad. Sci. USA* **110**, 20527–20532 (2013).
- Giordano, N., Mairet, F., Gouzé, J.-L., Geiselman, J. & de Jong, H. Dynamical allocation of cellular resources as an optimal control problem: novel insights into microbial growth strategies. *PLoS Comput. Biol.* **12**, e1004802 (2016).

**Supplementary Information** is available in the online version of the paper.

**Acknowledgements** We are grateful to E. Mateescu for initiating this work and to J. Hasty and R. Young for discussions. This work is supported by the National Institutes of Health (NIH; grant 1R01GM109069) and by the Simons Foundation (grant 330378) through T.H., by the NIH (grant 1R01GM118850) through J.R.W., and by the German Research Foundation via the Excellence Cluster 'Nanosystems Initiative Munich' and the priority program SPP1617 (grant GE1098/6-2) through U.G.

**Author Contributions** D.W.E., S.J.S., U.G. and T.H. designed this study. Growth shifts were performed by D.W.E. and S.J.S. and analysed by S.J.S., D.W.E. and T.H. Quantitative mass spectrometry analysis was performed by V.P. and analysed by S.J.S., V.P. and J.R.W. D.W.E., S.J.S., U.G. and T.H. developed the model and all authors participated in writing the paper and the Supplementary Information.

**Author Information** Reprints and permissions information is available at [www.nature.com/reprints](http://www.nature.com/reprints). The authors declare no competing financial interests. Readers are welcome to comment on the online version of the paper. Publisher's note: Springer Nature remains neutral with regard to jurisdictional claims in published maps and institutional affiliations. Correspondence and requests for materials should be addressed to T.H. ([hwa@ucsd.edu](mailto:hwa@ucsd.edu)) or U.G. ([gerland@tum.de](mailto:gerland@tum.de)).

## METHODS

No statistical methods were used to predetermine sample size. The experiments were not randomized and the investigators were not blinded to allocation during experiments and outcome assessment.

**Growth medium.** All growth media used in this study were based on N–C–minimal medium<sup>29</sup>, containing K<sub>2</sub>SO<sub>4</sub> (1 g), K<sub>2</sub>HPO<sub>4</sub>·3H<sub>2</sub>O (17.7 g), KH<sub>2</sub>PO<sub>4</sub> (4.7 g), MgSO<sub>4</sub>·7H<sub>2</sub>O (0.1 g), and NaCl (2.5 g) per litre. The medium was supplemented with 20 mM NH<sub>4</sub>Cl as the nitrogen source, and various carbon sources. 1 mM IPTG was added to media when necessary to fully induce the native *lac* operon, or 0.1 mM IPTG was added to induce the P<sub>Llac-O1</sub> promoter driving XylR for titratable expression of *dctA* in strain NQ537. The expression of the *Pu* promoter was activated by the regulator XylR upon induction by 3-methylbenzyl alcohol (3MBA), added at indicated concentrations. Extended Data Fig. 1h, i include steady-state growth rates supported by the medium for all carbon sources used.

**Culture procedure.** Each experiment was carried out in three steps: seed culture, pre-culture and experimental culture. Cells taken from –80 °C glycerol stock were seeded on an LB Agar plate before the experiment. A single colony was picked and grown on fresh LB in a shaken water bath at 37 °C and 250 r.p.m. Media in the pre-culture were chosen to be identical to the experimental culture. Inoculation of the pre-culture with washed seed culture was chosen such that the pre-culture grown overnight were still growing exponentially on the morning of the experiment. Cells were kept for at least ten doublings (at least five for growth rates below 0.4 h<sup>-1</sup>) in the pre-culture at 37 °C, shaken at 250 r.p.m. Inoculation into pre-warmed experimental culture in the morning was chosen such that cells spent at least an additional 3 doublings at 37 °C with shaking at 250 r.p.m. in the experimental culture before growth was measured.

For small culture volumes, 5 ml of experimental culture was grown in 20 mm × 150 mm glass test tubes. For larger volumes, 25 ml (100 ml) was grown in 125 ml (500 ml) baffled Erlenmeyer flasks. At each time point, a 200-μl sample was extracted and the optical density was measured using a 1 mm path length Starna Sub-Micro cuvette at 600 nm in a ThermoScientific Genesys 20 spectrophotometer.

High-precision optical density data shown in Fig. 1 were obtained using a flow-cell set-up. An experimental culture, 25 ml in volume, was shaken at 37 °C and 250 r.p.m. in a 125 ml baffled Erlenmeyer flask in an air incubator. A peristaltic pump was used to circulate medium through a flow-cell cuvette. OD<sub>600 nm</sub> was measured using an LED light source (592 nm) and a photodetector controlled by a microcontroller. All instruments and tubing were kept at 37 °C inside the air incubator.

**Strains.** All strains used in this study are derived from wild-type *E. coli* K-12 strain NCM3722<sup>30</sup> and are summarized in Extended Data Fig. 1j. Titratable *dctA* expression strain was constructed as described previously<sup>15</sup>. In brief, the region containing the *km* gene and *Pu* promoter was PCR-amplified from plasmid pKDPu and integrated into the chromosome of *E. coli* strain NQ351 upstream of *dctA* (–1 to –182 bp relative to translational start point of *dctA*), by using the λ Red system<sup>31</sup>. The resulting *km-Pu-dctA* in the above strain was transferred into strain NQ386 containing P<sub>Llac-O1-xylR</sub> by P1 transduction, resulting in strain NQ530. To construct a titratable *lacZ* expression strain, *km-Pu-lacZ* in Supplementary equation (40) was transferred into strain NQ386 by P1 transduction, resulting in strain NQ537. Strains NQ381 and NQ399 have been described previously<sup>16</sup>. A *dctA* knockout was transferred from JW3496-1 to NCM3722 via P1 transduction to yield strain NQ1324.

**β-galactosidase quantification.** The β-galactosidase quantification is based on the Miller assay<sup>32</sup> and used as described previously<sup>15</sup>.

**Total RNA quantification.** The RNA quantification method is based on the method used as described previously<sup>33</sup> with modifications as described<sup>15</sup>.

**Total protein quantification.** Total protein was quantified using a commercial microBCA assay. In summary, 1 ml samples were collected via centrifugation and stored at –80 °C until the analysis. For the analysis, cells were washed again and resuspended in N–C– medium and diluted 1:10. Next, 200 μl of diluted sample and 200 μl of microBCA working reagent were incubated at 60 °C in a water bath. After 1 h, samples were put on ice, cell debris was removed via centrifugation and absorbance at 592 nm was recorded. Each analysis was calibrated individually using bovine albumin serum standards.

**Dry mass quantification.** 150 ml cell culture was grown in baffled 250 ml flasks to an OD<sub>600 nm</sub> of about 0.5 at 37 °C in a water-bath shaker. Triplicates of 50 ml cell culture were subsequently collected, cooled by shaking in an ice–water bath, and concentrated via centrifugation. Supernatants were recorded at every step and subtracted from the OD<sub>600 nm</sub> reading. The resulting pellet was transferred to 1.5 ml tubes and dried at 80 °C overnight. The resulting mass of the pellet was determined with a high-precision balance.

**Growth transition mass spectrometry protocol.** We used quantitative mass spectrometry to analyse the kinetic series of the up- and downshift shown in

Fig. 1. Over approximately two doublings, we collected two pre-shift and six logarithmically spaced post-shift samples for each kinetic transition, each containing the equivalent biomass of 1 ml liquid culture at OD<sub>600 nm</sub> = 1, collected by centrifugation at 17,000g for 2 min. To enable light/heavy relative quantitation using mass spectrometry, we prepared a <sup>15</sup>N stable-isotope labelled reference containing a 1:1 (w/w) mixture of steady-state glucose and succinate-minimal medium cultures grown in the presence of <sup>15</sup>NH<sub>4</sub>Cl.

After resuspension in pure water, 100 μl of the mixed <sup>15</sup>N reference containing the equivalent of 1 ml liquid culture at OD<sub>600 nm</sub> = 1 cell biomass was added to each sample cell pellet previously stored at –20 °C. Subsequent sample processing, including TCA precipitation, cysteine reduction, alkylation, tryptic digestion, and desalting procedures, was performed as previously described<sup>24</sup>.

Tryptic peptides were separated on an Eksigent NanoLC Ultra system coupled to a Sciex 5600 TripleTOF system and analysed in data-dependent shotgun mode (250 ms MS1 scan, followed by 40 cycles of 150 ms MS2 scans)<sup>24</sup>. Each sample was injected twice, yielding two technical replicates.

As described previously<sup>24</sup>, vendor WIFF-format instrument data files were converted to profile and centroid MZML formats using Sciex software. Using the Trans-Proteomic Pipeline<sup>34</sup>, centroided mzML files were converted to mzXML and searched using X!Tandem<sup>35</sup> against a custom *E. coli* database (derived from UniProt organism 83333). The MS2 search results were combined into raw and consensus spectral libraries using SpectraST.

MS1 intensity envelopes containing <sup>14</sup>N (light)- and <sup>15</sup>N (heavy)-labelled ions were fit using a least-squares Fourier transform convolution algorithm<sup>19</sup> implemented using isodist<sup>36</sup> as implemented in the Perl program massacre<sup>37</sup>. Relative <sup>14</sup>N/<sup>15</sup>N ratios were corrected for unbalanced <sup>15</sup>N-reference pipetting by the quotient of the cumulative light (sample) and heavy (reference) X!Tandem spectral counts for *E. coli* peptides on a per-sample basis. Absolute protein expression (that is, the fraction of the total protein mass that is a specific protein) was estimated by spectral counting of X!Tandem peptide–spectrum matches.

For each upshift and downshift, the time series of ‘absolute expression data’ can be represented in the form of an expression matrix  $E_{m,n}$ , with the time series ( $n = 1 \dots 8$ ) along the columns, and the number of proteins,  $m$ , as rows.

Proteins previously classified to increase, decrease or show no response under carbon limitation<sup>19</sup> were classified as the C<sub>↑</sub>, C<sub>↓</sub> and C<sup>–</sup> sectors. 24 proteins not detected previously<sup>19</sup> were classified according to the nearest distance of their linear response (average of both upshift and downshift) and the average linear response of proteins belonging to each sector.

Data shown in Fig. 4a use relative expression data, which were obtained by normalizing the ‘absolute expression data’ to the pre-shift expression data (average of one data point at  $t = -15$  min, and a second data point immediately before the shift). If both pre-shift entries were empty, data could not be normalized and were removed from the analysis. Additionally, to focus on high-quality expression data, rows (protein) with more than four empty entries were removed, yielding a total of  $m = 647$  proteins, which are provided in Supplementary Table 1. Data were log<sub>2</sub> transformed and plotted as a heat map in Fig. 4a.

Data shown in Fig. 4b, c use ‘absolute expression data’ (that is, absolute mass fractions of proteins). Single-protein data are provided in Supplementary Table 2. The abundance of a sector  $X$  at time entry  $n$ ,  $\varphi_{X,n}$ , was calculated by summing protein expression  $p_{m,n}$  over all entries  $m$ , under the condition that protein  $m$  is an element of the sector  $X$ , and is provided in Supplementary Table 3. Protein groups were calculated analogously to the protein sectors; the mass fraction of all protein groups was approximately 60% of the proteome. Data are provided in Supplementary Table 4. Classifications of proteins (sectors and groups) are provided in Supplementary Table 1.

**Pulse-labelling mass spectrometry protocol.** Cells were grown in N–C– medium with 10 mM <sup>14</sup>NH<sub>4</sub>Cl as the sole source of nitrogen. At the time of glucose exhaustion (downshift) and gluconate addition (upshift), cells were <sup>15</sup>N-isotopically labelled by adding a pulse of <sup>15</sup>NH<sub>4</sub>Cl to 10 mM. The pulse allows the differentiation of protein made pre-shift (<sup>14</sup>N) from protein made post-shift (50% <sup>15</sup>N). We collected two pre-shift and six post-shift samples (1 OD<sub>600 nm</sub> × ml total biomass) for each series. A <sup>15</sup>N-isotopically enriched reference was prepared as a 1:1 (w/w) mixture of steady-state succinate- and glucose-minimal-medium cultures grown in the presence of <sup>15</sup>NH<sub>4</sub>Cl and added to each sample as above.

Data acquisition and processing were performed as described in ‘Growth transition mass spectrometry protocol’.

MS1 intensity envelopes containing <sup>14</sup>N-labelled (pre-shift) ions, 50% <sup>15</sup>N (post-shift) ions, and 100% <sup>15</sup>N-labelled (constant reference) ions were quantified using isodist<sup>36</sup> to fit a three-species model, including the 50% <sup>15</sup>N-labelled envelope.

**Application of the FCR model to specific growth shifts.** The FCR model is built on the steady-state growth laws (Supplementary equations (9) and (12)), shown in Extended Data Fig. 1c, d and discussed in Supplementary Note 2), which serve as the general input to the model, independent of specific growth shifts. The constants

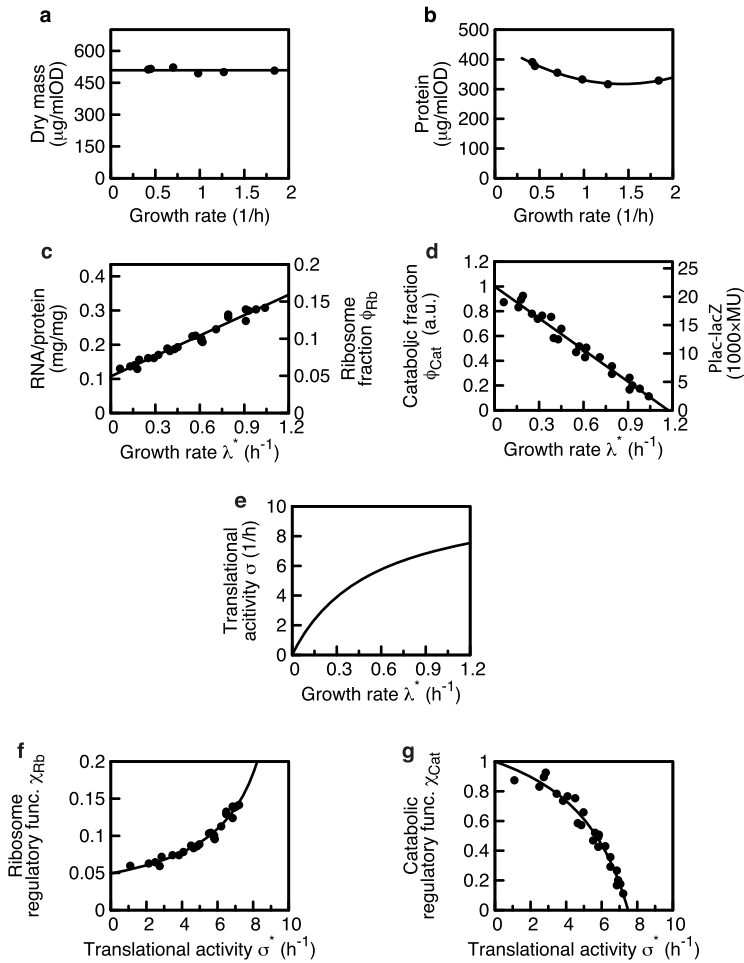
appearing in the linear growth laws ( $\varphi_{\text{Rb},0}$ ,  $\gamma$ ,  $\lambda_C$ ) fix the parameters appearing in the regulatory functions  $\hat{\chi}_{\text{Cat}}$  and  $\hat{\chi}_{\text{Rb}}$  (Supplementary equations (28) and (29)), which enter the central equation of the translational activity  $\sigma(t)$  in equation (5) (or Supplementary equation (43)). Additionally, the FCR model requires growth-shift-specific parameters: the initial growth rate  $\lambda_i$  and the final growth rate  $\lambda_f$ . The final growth rate  $\lambda_f$  fixes the parameter  $\mu_f$  (appearing in equation (5)), which describes the quality of the post-shift nutrient, via the growth laws (Supplementary equation (17)).

The initial condition of the translational activity  $\sigma(0)$ , as defined in Supplementary equation (50), is determined by the type of shift, and can lead to markedly different transition kinetics. For upshifts without pre-expression between co-utilized carbon sources, the initial condition  $\sigma(0)$  equals the pre-shift value  $\sigma_i$ , determined by the pre-shift growth rate,  $\lambda_i$ ; see Supplementary equation (52). For upshift with pre-expression, the initial condition  $\sigma(0)$  requires fitting of the pre-expression level, see Supplementary equation (54). For downshifts between co-utilized carbon substrates, the initial condition  $\sigma(0)$  is set by the carbon influx of the remaining substrate, which can be calculated from the initial and final growth rates,  $\lambda_i$  and  $\lambda_f$ , and the growth laws, see Supplementary equation (56). For downshifts between hierarchically used carbon substrates, the initial condition  $\sigma(0)$  requires fitting one parameter.

Pre-shift growth of all variables is determined by the initial growth rate  $\lambda_i$  and the growth laws, see Supplementary equations (58)–(64). Post-shift growth is calculated from the time-dependent solution of  $\sigma(t)$  (obtained analytically as Supplementary equation (49)); the solution is used to derive the general analytical solutions for all other dynamic quantities, including the abundance of ribosomes ( $M_{\text{Rb}}(t)$ , Supplementary equation (66)) catabolic protein ( $M_{\text{Cat}}(t)$ , Supplementary equation (73)), biomass synthesis ( $J_{\text{R}}(t)$ , Supplementary equation (68)), biomass ( $M(t)$ , Supplementary equation (76)), and growth rate ( $\lambda(t)$ , Supplementary equation (77)); see Supplementary Note 4.4 for the derivation of these results. If carbon uptake is substrate-limited (Supplementary equations (19) and (20)), as occurs when the concentration of a substrate is reduced to very low levels, then the model can only be solved numerically (Supplementary Note 4).

**Data availability.** The data that support the findings of this study are available from the corresponding author upon reasonable request.

29. Csonka, L. N., Ikeda, T. P., Fletcher, S. A. & Kustu, S. The accumulation of glutamate is necessary for optimal growth of *Salmonella typhimurium* in media of high osmolality but not induction of the *proU* operon. *J. Bacteriol.* **176**, 6324–6333 (1994).
30. Soupene, E. *et al.* Physiological studies of *Escherichia coli* strain MG1655: growth defects and apparent cross-regulation of gene expression. *J. Bacteriol.* **185**, 5611–5626 (2003).
31. Datsenko, K. A. & Wanner, B. L. One-step inactivation of chromosomal genes in *Escherichia coli* K-12 using PCR products. *Proc. Natl Acad. Sci. USA* **97**, 6640–6645 (2000).
32. Miller, J. H. *Experiments in Molecular Genetics* (Cold Spring Harbor Laboratory Press, 1972).
33. Benthin, S., Nielsen, J. & Villadsen, J. A simple and reliable method for the determination of cellular RNA content. *Biotechnol. Tech.* **5**, 39–42 (1991).
34. Deutsch, E. W. *et al.* A guided tour of the Trans-Proteomic Pipeline. *Proteomics* **10**, 1150–1159 (2010).
35. Craig, R. & Beavis, R. C. TANDEM: matching proteins with tandem mass spectra. *Bioinformatics* **20**, 1466–1467 (2004).
36. Sperling, E., Bunner, A. E., Sykes, M. T. & Williamson, J. R. Quantitative analysis of isotope distributions in proteomic mass spectrometry using least-squares Fourier transform convolution. *Anal. Chem.* **80**, 4906–4917 (2008).
37. Sykes, M. T., Sperling, E., Chen, S. S. & Williamson, J. R. Quantitation of the ribosomal protein autoregulatory network using mass spectrometry. *Anal. Chem.* **82**, 5038–5045 (2010).
38. Schaechter, M., Maaløe, O. & Kjeldgaard, N. O. Dependency on medium and temperature of cell size and chemical composition during balanced growth of *Salmonella typhimurium*. *J. Gen. Microbiol.* **19**, 592–606 (1958).
39. Basan, M. *et al.* Inflating bacterial cells by increased protein synthesis. *Mol. Syst. Biol.* **11**, 836 (2015).
40. Tong, S., Porco, A., Isturiz, T. & Conway, T. Cloning and molecular genetic characterization of the *Escherichia coli gntR*, *gntK*, and *gntU* genes of GntI, the main system for gluconate metabolism. *J. Bacteriol.* **178**, 3260–3269 (1996).
41. Voegelé, R. T., Sweet, G. D. & Boos, W. Glycerol kinase of *Escherichia coli* is activated by interaction with the glycerol facilitator. *J. Bacteriol.* **175**, 1087–1094 (1993).
42. Dennis, P. P. & Bremer, H. Differential rate of ribosomal protein synthesis in *Escherichia coli* B/r. *J. Mol. Biol.* **84**, 407–422 (1974).



**h**

Carbon substrate	Growth rate (1/h)	LacZ activity (MU)	Rb-protein/Tot. protein
20 mM proline	0.13	-	0.063
0.1% mannose	0.19	20177	0.072
0.2% fructose	0.61	10756	0.097
20 mM gluconate	0.91	5772	0.139
0.2% glucose	0.91	3636	0.124
0.2% glycerol	0.62	11069	0.096
20 mM OAA	0.79	7761	0.133
20 mM OAA + 0.2% glucose	1.04	2474	0.142
20 mM OAA + 0.2% glycerol	0.93	4389	0.138
20 mM pyruvate	0.71	9364	0.113
20 mM succinate	0.45	14356	0.089
20 mM succinate + 20 mM gluconate	0.98	3790	0.140

**i**

Strain	Carbon substrate	3MBA (μM)	Growth rate (1/h)	LacZ activity (MU)	Rb-protein/Tot. protein
NQ530	20 mM succinate	25	0.06	19077	0.060
		50	0.16	18094	0.065
		100	0.25	17061	0.073
-----					
NQ381	0.2% lactose	500	0.40	12758	0.084
		0	0.29	16093	0.074
		25	0.43	12514	0.086
NQ399	0.2% glycerol	50	0.55	10194	0.103
		100	0.61	9295	0.100
		500	0.79	6399	0.129
-----					
NQ399	0.2% glycerol	25	0.18	19499	0.059
		50	0.32	16688	0.078
		100	0.38	16468	0.086
500	0.57	11308	0.105		

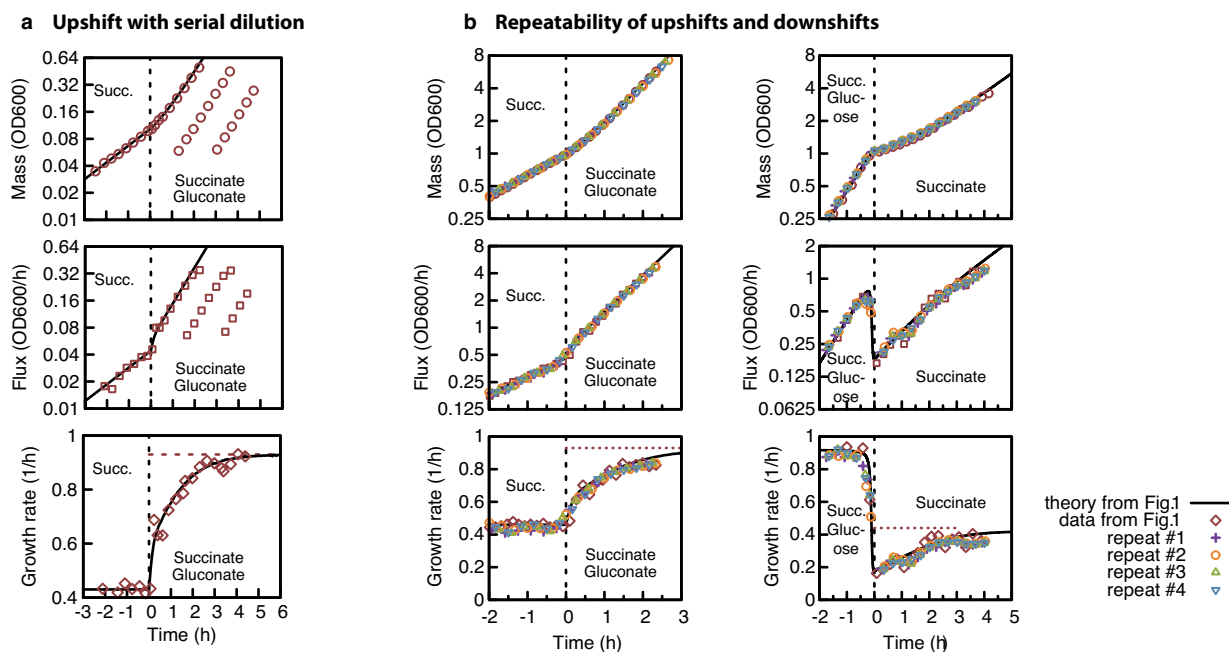
**j**

Strain name	Genotyp	ncestor	Function
NCM3722	-	-	Wild-type
NQ381	attB::PLlac-O1-xyIR, lacY::km-Pu-lacY	NCM3722	Titrateable <i>lacY</i>
NQ399	attB::PLlac-O1-xyIR, PglpFK::km-Pu	NCM3722	Titrateable <i>glpFK</i>
NQ530	attB::PLlac-O1-xyIR, PdctAK::km-Pu	NCM3722	Titrateable <i>dctA</i>

**Extended Data Figure 1 | Growth laws.** **a**, Dry mass per optical density  $OD_{600\text{ nm}}$  is independent of the growth rate in the investigated conditions with an average of  $509\ \mu\text{g}$  dry weight per  $\text{ml} \times OD_{600\text{ nm}}$  value (black line). **b**, Protein mass per optical density  $OD_{600\text{ nm}}$  shows a slight dependence on growth rate (black line: guide to the eye), in accordance with the increase of RNA and DNA in the cell at higher growth rates<sup>38</sup>. Because the change is small in the range of growth rates of the up- and downshifts presented, we take the conversion from dry mass to total protein to be constant throughout the shifts presented. Dry mass and total protein data taken from ref. 39. **c**, Ribosomal proteome fraction of the cell  $\phi_{\text{Rb}}^*(\lambda^*)$  at steady-state growth at rate  $\lambda^*$ , using RNA or protein as a reporter. The data are fitted with the linear relation  $\phi_{\text{Rb}}^* = \phi_{\text{Rb},0} + \lambda^*/\gamma$  with

$\phi_{\text{Rb},0} = (0.049 \pm 0.02)$  and  $\gamma = (11.02 \pm 0.44)\ \text{h}^{-1}$ . **d**, Catabolic proteins ( $\phi_{\text{Cat}}^*(\lambda^*)$ , left axis) were measured with LacZ (induced with 1 mM IPTG) as a reporter and measuring Miller units (MU) (right axis; see ref. 32 for MU). The linear relation was fitted with  $\phi_{\text{LacZ}}^* = \phi_{\text{LacZ,max}}^*(1 - \lambda^*/\lambda_{\text{C}})$  with  $\phi_{\text{LacZ,max}}^* = (21.8 \pm 0.5) \times 10^3\ \text{MU}$  and  $\lambda_{\text{C}} = (1.17 \pm 0.05)\ \text{h}^{-1}$ . **e**, The translational activity  $\sigma^*$  is calculated from  $\phi_{\text{Rb}}^*(\lambda^*)$  (**c**) as  $\sigma^* = \lambda^*/\phi_{\text{Rb}}^*(\lambda^*)$ . **f**, **g**, Regulatory functions  $\hat{\chi}_{\text{Rb}}(\sigma^*)$  and  $\hat{\chi}_{\text{Cat}}(\sigma^*)$ , functions of the translational activity  $\sigma^*$ , are calculated by substituting  $\lambda^*$  by  $\sigma^*$  from the fits in **c** and **d** (see Supplementary Equations (28) and (29)). **h**, **i**, Tables show all data plotted in **c** and **d**. Data in **h** were measured by growth on different carbon substrates, data in **i** were measured by growth of strains with titrateable transporter expression, see list of strains in **j**.

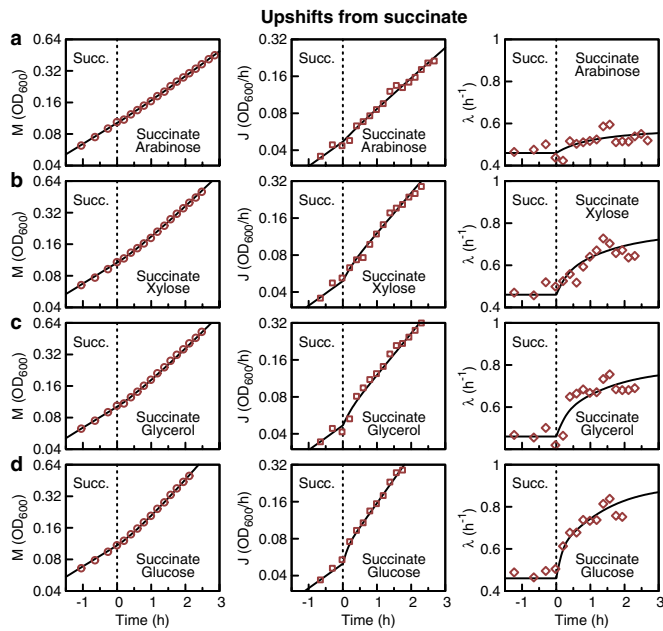




### Extended Data Figure 2 | Long-term dynamics and repeatability.

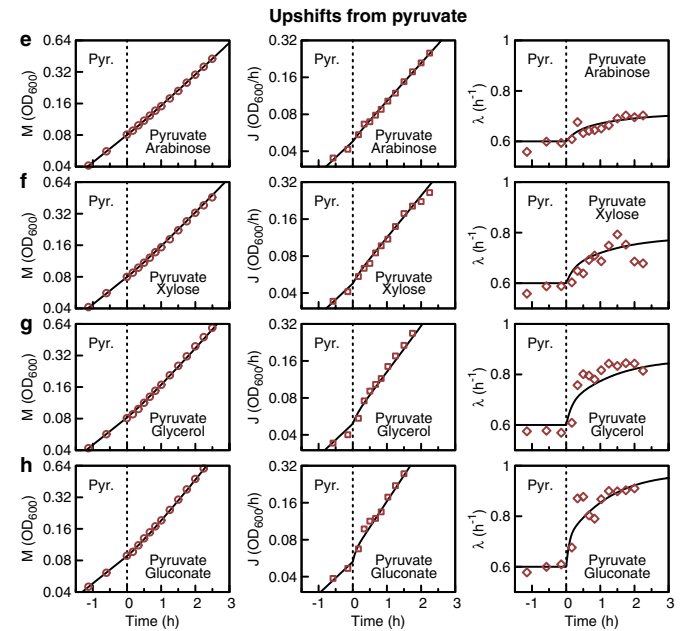
**a**, Serial dilution experiment of the upshift of Fig. 1 (succinate, add gluconate). The top graph shows optical density  $OD_{600\text{ nm}}$  as a measure of biomass  $M(t)$ , the middle graph shows biomass flux  $J(t)$ , and the bottom graph shows the growth rate  $\lambda(t) = J(t)/M(t)$ . Shortly after the upshift, the cell culture was diluted 4- and 16-fold in fresh medium, grown in parallel to the original culture, and the optical density was recorded for the diluted cultures once they reached an optical density of around 0.05. As the

growth rate is independent of the cell density, data from the original and the diluted cultures collapse, showing that for longer times the growth rate reaches its final level (dashed line). **b**, Repeatability. Biomass (top), flux (middle) and growth rate (bottom) for (left to right) the upshift from Fig. 1a–e and the downshift shown in Fig. 1f–j. Theory (black line) and data (red diamonds) are identical to Fig. 1. Four independent repeats (purple, orange, green and blue) are plotted on top of the data shown in Fig. 1.

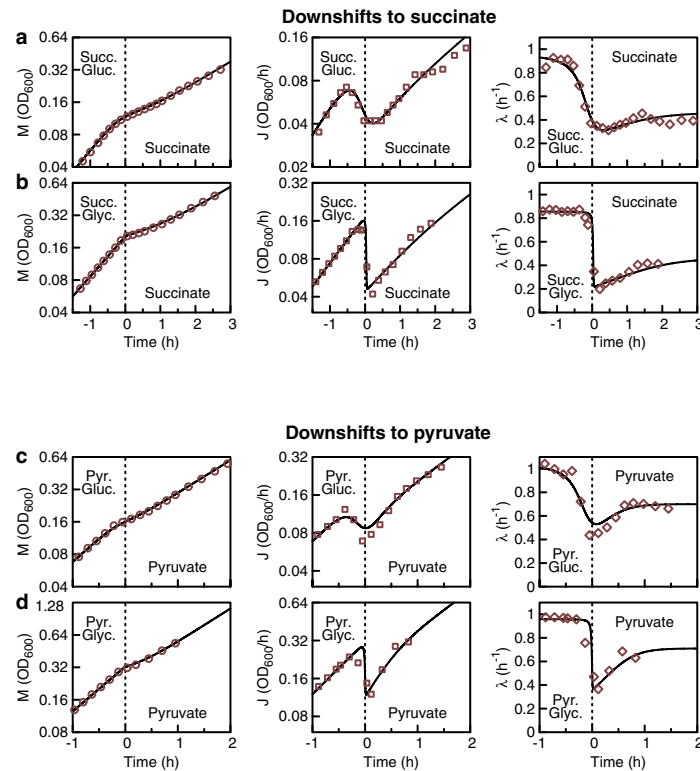


### Extended Data Figure 3 | Upshifts from succinate and pyruvate.

**a–h**, NCM3722 grown exponentially on 20 mM succinate (succ.) or 20 mM pyruvate (pyr.) as the sole carbon substrate. At  $t = 0$  a second, subsequently co-utilized carbon substrate was added: 0.2% arabinose (**a**, **e**); 0.2% xylose (**b**, **f**); 0.2% glycerol (**c**, **g**); 0.2% glucose (**d**); 20 mM gluconate (**h**). The left panels show optical density  $OD_{600\text{ nm}}$  (a measure of biomass  $M(t)$ , red circles), the middle panels show the derivative of

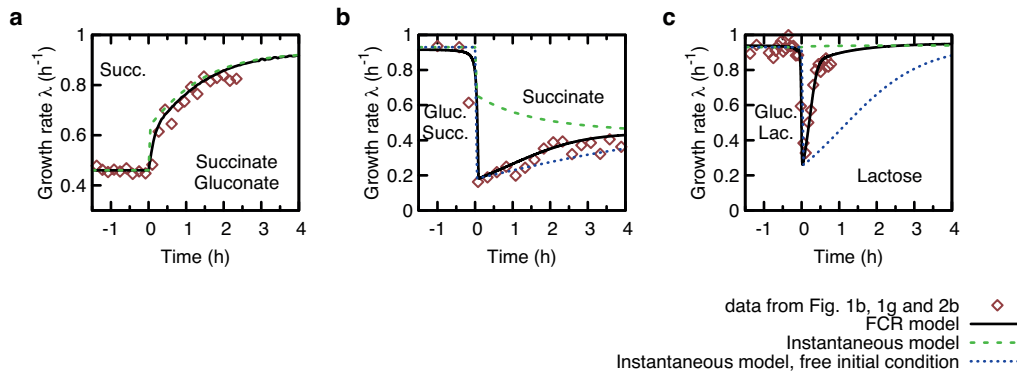


$OD_{600\text{ nm}}$  (a measure for biomass flux  $J(t)$ , red squares), and the right panels show growth rate ( $\lambda(t) = J(t)/M(t)$ , red diamonds). Theory lines for  $M(t)$ ,  $J(t)$  and  $\lambda(t)$  were calculated using Supplementary equations (76), (70) and (77), using the initial condition Supplementary equation (52) for upshift without pre-expression. Initial and final growth rates were measured during steady-state growth on the respective carbon substrates.



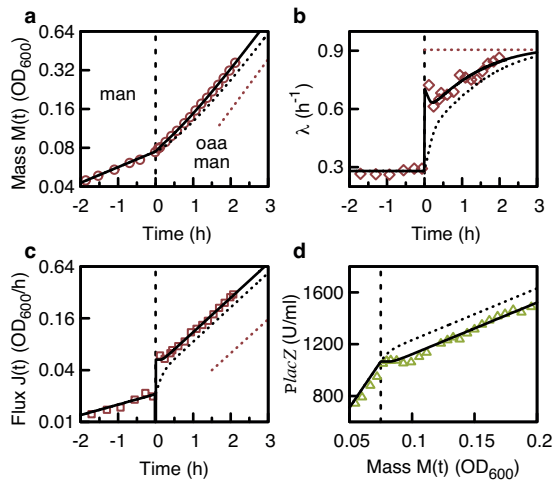
**Extended Data Figure 4 | Downshift with co-utilized carbon substrates.** **a–d**, NCM3722 grown exponentially on 20 mM succinate (succ.) (**a**, **b**) or 20 mM pyruvate (pyr.) (**c**, **d**), combined with either 0.56 mM gluconate (gluc.) (**a**, **c**) or 1.11 mM glycerol (glyc.) (**b**, **d**). At around  $t = 0$ , gluconate or glycerol were depleted. The left panels show optical density  $OD_{600\text{ nm}}$  (a measure of biomass  $M(t)$ , red circles), middle panels show the derivative of  $OD_{600\text{ nm}}$  (a measure for biomass flux  $J(t)$ , red squares), and right panels show the growth rate ( $\lambda(t) = J(t)/M(t)$ , red diamonds). Theory lines for  $M(t)$ ,  $J(t)$  and  $\lambda(t)$  were calculated solving the differential equation for

the translational activity  $\sigma(t)$  (Supplementary equation (22)), and those defining the internal fluxes and protein content (Supplementary equations (19)–(21) and (22)–(24)) numerically. The uptake of the depleting substrate (glycerol or gluconate) was calculated from Supplementary equation (20), using the Michaelis constants  $K_m = 212\ \mu\text{M}$  (gluconate<sup>40</sup>) and  $K_m = 5.6\ \mu\text{M}$  (glycerol<sup>41</sup>). Since gluconate transport has a low affinity, it depletes slowly (see **a** and **c**), which is accurately described by our modelling of catabolism. Initial and final growth rates were measured during steady-state growth on the respective carbon substrates.

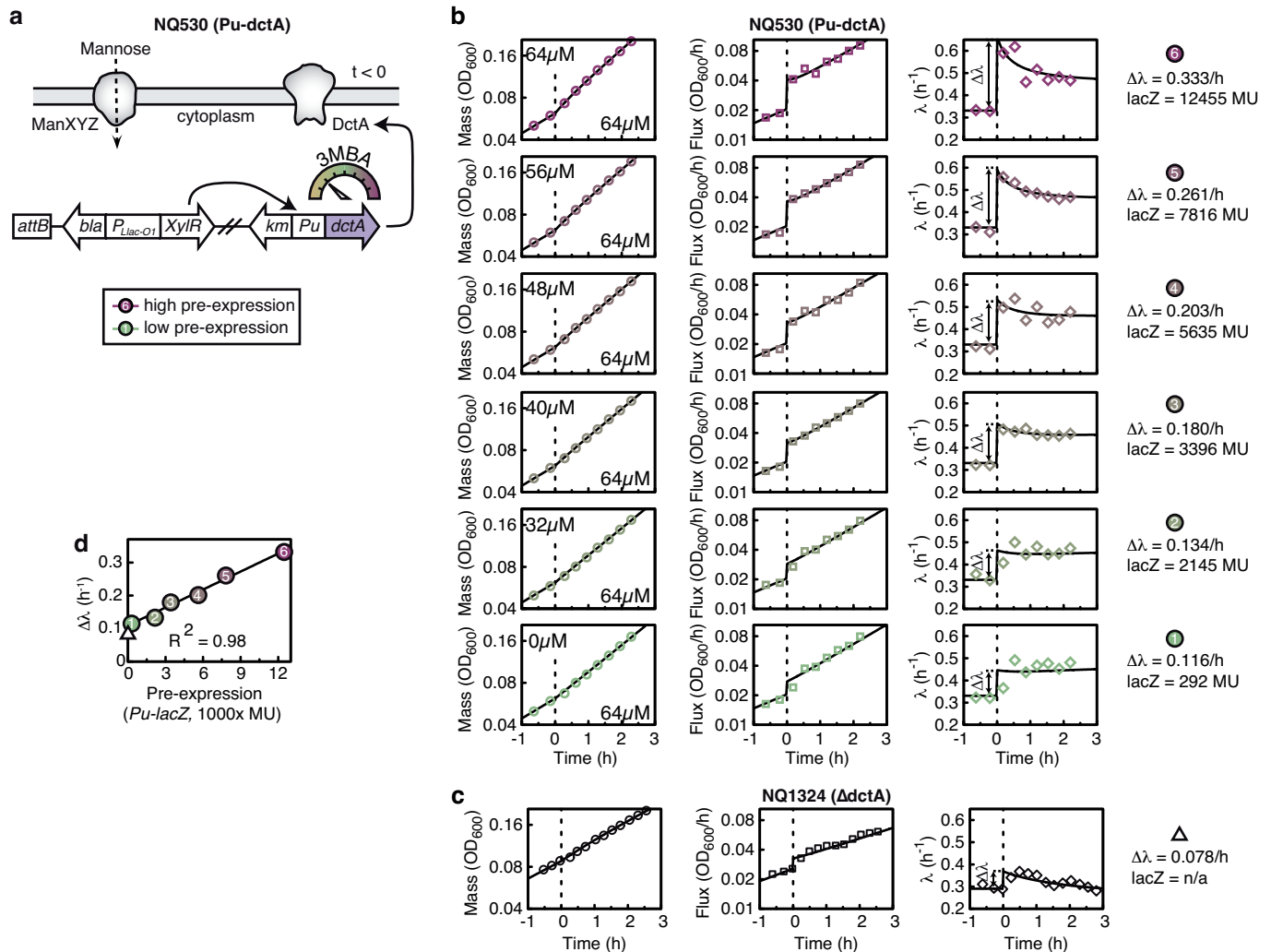


**Extended Data Figure 5 | Performance of models of growth kinetics without gene regulation.** a–c, This figure shows the result of three nutrient shifts discussed in the main text: Succinate–gluconate upshift from Fig. 1b (a); Succinate–glucose downshift from Fig. 1g (b); Glucose–lactose diauxic shift from Fig. 3b (c). Experimental data are shown as red symbols. Among existing models of growth transition, the one proposed by Dennis and Bremer allows for predicting growth transitions of upshifts<sup>42</sup>. This model assumes that the flux jumps instantaneously to the final state without a regulatory scheme (see Supplementary Note 1 for a review). Predictions of this model, referred to here as the ‘instantaneous

model’, are shown as the green dashed lines in all panels. Although the instantaneous model works well for upshifts (panel a), for which it was developed<sup>42</sup>, it fails to describe downshifts (panels b and c), because it cannot describe a flux decrease. The instantaneous model cannot be fixed by matching the flux after glucose depletion (blue dotted lines in panels b and c), as it underestimates the recovery rate owing to a lacking regulatory scheme (Supplementary Note 1). By contrast, the FCR model introduced in this work, based on an active reallocation of protein synthesis during growth transitions, predicts the correct recovery rates (black solid lines) consistently for both up- and downshifts.



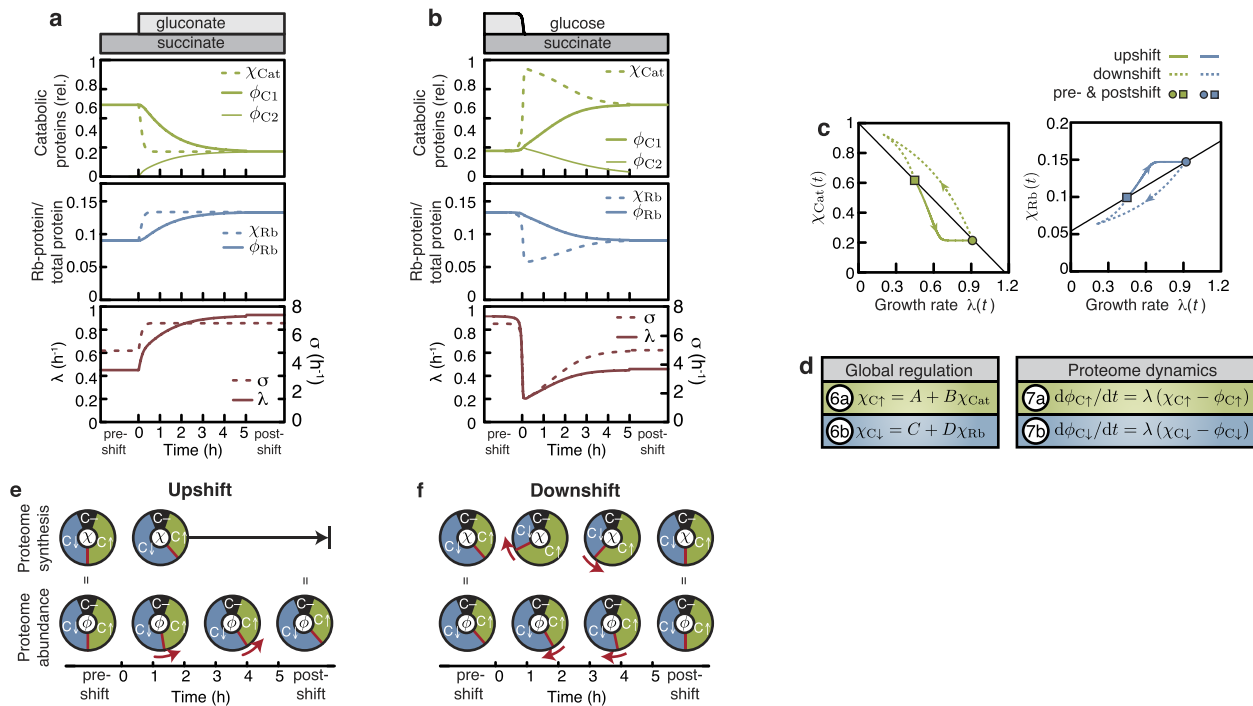
**Extended Data Figure 6 | Upshift from mannose.** **a–c**, NCM3722 grown exponentially on 0.1% mannose as the sole carbon substrate. At  $t = 0$  (dashed line) oxaloacetic acid (OAA), subsequently co-utilized, is added. Optical density  $OD_{600\text{ nm}}$  (a measure of biomass  $M(t)$ , red circles) (**a**), the derivative of  $OD_{600\text{ nm}}$  (a measure of biomass flux  $J(t)$ , red squares) (**b**), growth rate ( $\lambda(t) = J(t)/M(t)$ , red diamonds) (**c**). **d**, Expression of the catabolic proteins reporter LacZ is transiently repressed after the shift (vertical dashed line). Dotted black lines show solutions of the theory using the initial condition for no pre-expression (Supplementary equation (52)), which does not coincide with the experimental data (symbols). Using the initial condition for pre-expression (Supplementary equation (54)) and fitting the pre-expression level, the theory (black lines) describes the data very well, including the transient repression of LacZ in **d**. LacZ activity units U are defined as  $MU \times OD_{600\text{ nm}}$ .



### Extended Data Figure 7 | Effect of pre-expression on upshift kinetics.

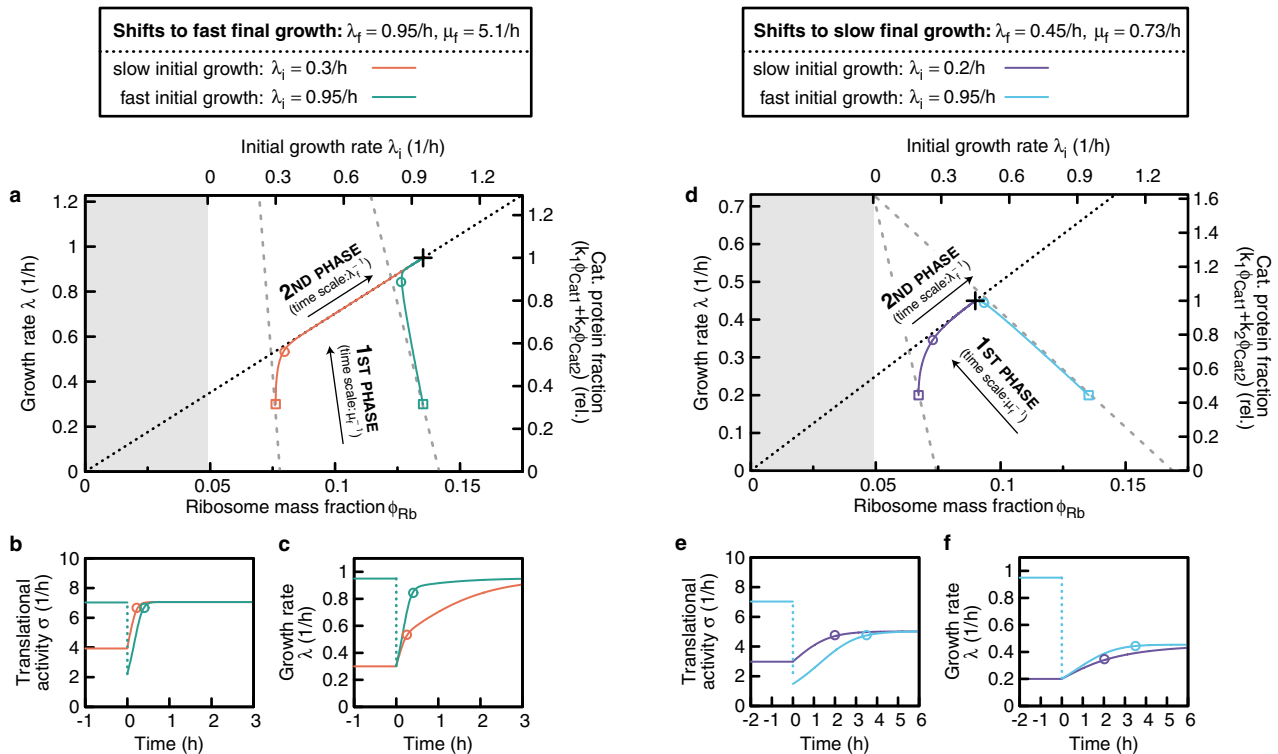
**a**, *E. coli* NQ530 grown exponentially in mannose minimal medium with different levels of succinate transporter (DctA) pre-expressed via the titratable *Pu* promoter (regulator: XylR, inducer: 3MBA). At time  $t = 0$ , medium was supplemented with 20 mM succinate and DctA expression is set to a common level for all upshifts. **b**, Biomass  $M(t)$  ( $OD_{600\text{ nm}}$ ), biomass flux  $J(t)$  (derivative of  $OD_{600\text{ nm}}$ ) and growth rate  $\lambda(t)$  for different levels of pre-expression (3MBA concentration indicated in panels). DctA pre-expression positively affects post-shift growth. The biomass flux  $J(t)$  (middle) shows a saltatory increase followed by exponential growth at final rate  $\lambda_f$ . For cultures with a high level of pre-expression, the instantaneous growth rate  $\lambda(t)$  (right) transiently overshoots before relaxing to the final value  $\lambda_f$ . The increase is transient because the DctA level in the synthetic

construct eventually decreases below the pre-expression level. The kinetic theory quantitatively captures the upshift kinetics for all pre-expression levels, when using the initial condition  $\sigma(0)$  as the single fit parameter (solid lines). **c** NQ 1324 ( $\Delta$ dctA) shows a small increase in growth rate upon upshift, despite the succinate transporter DctA being knocked out. Final growth rate is not significantly increased over steady-state growth on mannose alone. Steady-state growth rate on succinate alone was barely detectable for NQ1324 ( $\lambda \lesssim 0.02/h$ ). **e**, Validation of theoretical prediction. The magnitude of saltatory increase in growth rate  $\Delta\lambda$  (indicated in the right panels of **b**, **c**) depends linearly on the pre-expression levels. The saltatory increase of the *dctA* knockout shown in **c** is indicated by a triangle.



**Extended Data Figure 8 | Proteome remodelling.** **a, b**, Regulatory functions  $\chi$  and protein fractions  $\varphi$  of catabolic proteins (relative to maximal expression), ribosomes (absorbance in mg RNA per mg protein) as well as growth rate  $\lambda(t)$  and translational activity  $\sigma(t)$  during growth shifts for the upshift and downshift of Fig. 1. Soon after upshift the regulatory functions of catabolic proteins  $\chi_{\text{Cat}}(t)$  and ribosomes  $\chi_{\text{Rb}}(t)$ , driven by the translational activity  $\sigma(t)$  (green, blue and red dashed lines), have relaxed to the final state (**a**). A new proteome is thus synthesized at the final ratio, leading to a slow convergence to the final state by growth-mediated dilution. The shortfalls of carbon influx after glucose depletion lead to an upregulation of  $\chi_{\text{Cat}}(t)$  and a downregulation of  $\chi_{\text{Rb}}(t)$ , driven by the translational activity  $\sigma(t)$  (green, blue and red dashed lines) (**b**). **c**, The regulatory functions  $\chi_{\text{Cat}}(t)$  and  $\chi_{\text{Rb}}(t)$ , set by the translational activity  $\sigma(t)$ , plotted versus growth rate  $\lambda(t)$ . Thin black lines show the

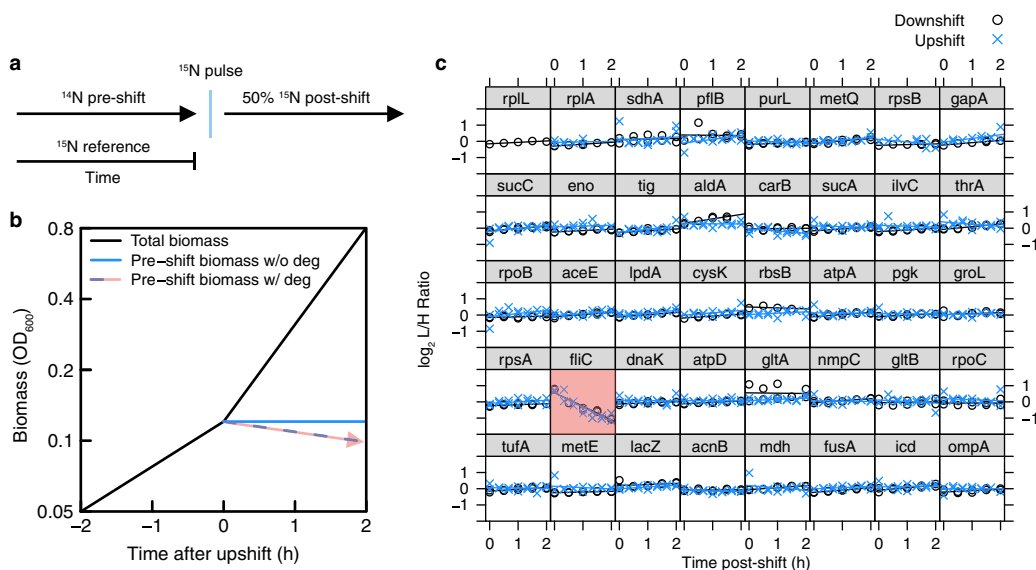
steady-state growth laws (Extended Data Fig. 1c, d and Supplementary Note 2). Despite the regulatory functions being derived from the growth laws (black lines), they diverge considerably during growth transitions, as they are controlled by the translational activity  $\sigma(t)$ , and not the growth rate  $\lambda(t)$ . **d**, Assuming co-regulation of the proteome sectors  $C_{\uparrow}$  and  $C_{\downarrow}$  with catabolic and ribosomal proteins (equations (6a) and (6b)), the dynamics of the proteome sectors can be described (equations (7a) and (7b); see Supplementary Note 5 for details). **e, f**, Graphical synopsis of the proteome remodelling of **a** and **b**, as predicted by equations (6a), (6b), (7a) and (7b). Red boundary and arrows show dynamics. In upshifts regulatory functions  $\chi$  rapidly relax to their final states; in downshifts regulatory functions initially overshoot and relax slowly to their final states (see Supplementary Note 6 for extended discussion).



**Extended Data Figure 9 | Biphasic relaxation kinetics.** The figure shows the relaxation kinetics for growth shifts, as obtained from the FCR model. **a–c**, An upshift from slow growth  $\lambda_i = 0.3 \text{ h}^{-1}$  (orange) and a downshift from fast pre-shift growth  $\lambda_i = 0.95 \text{ h}^{-1}$  (green) is seen, both with the same growth rate directly after the shift,  $\lambda(0) = 0.3 \text{ h}^{-1}$ , and the same fast final growth rate  $\lambda_f = 0.95 \text{ h}^{-1}$ . **d–f**, An upshift from slow growth  $\lambda_i = 0.2 \text{ h}^{-1}$  (orange) and a downshift from fast pre-shift growth  $\lambda_i = 0.95 \text{ h}^{-1}$  (green) is seen, with  $\lambda(0) = 0.2 \text{ h}^{-1}$ , and the same slow growth rate  $\lambda_f = 0.95 \text{ h}^{-1}$ . **a, d**, The trajectories of the recovery in the space of growth rate (left y-axis), which is proportional to the catabolic protein fraction (right y-axis), and ribosome fraction  $\phi_{Rb}(t)$  (bottom x-axis). The initial condition  $\phi_{Rb}(0)$  depends on the pre-shift growth rate  $\lambda_i$  (top x-axis). The trajectories start at the points  $(\phi_{Rb}(0), \lambda(0))$ , indicated by coloured squares, and end at the final state  $(\phi_{Rb,f}, \lambda_f)$ , marked with a black cross. As detailed in Supplementary Note 6, the kinetics are biphasic and can be understood using a simple geometric construction, which yields the dotted and dashed lines (see Supplementary Note 6.2). First, a relaxation associated with a timescale  $\mu_f^{-1}$  (Supplementary equation (116)), along the

grey dashed lines, during which protein synthesis contains more catabolic proteins and fewer ribosomes than the final composition of the proteome. The end of this kinetic phase is indicated by circles in all panels. Second, a slow motion along the diagonal dashed line on the timescale  $\lambda_f^{-1}$  (Supplementary equation (120)). Along this line, the translational activity,  $\sigma(t) = \lambda(t)/\phi_{Rb}(t)$ , has relaxed to the final state (see **b, e**), where  $\sigma(t)$  has relaxed after the 'circles'. As a result, the regulatory functions have relaxed to the final state too, and protein synthesis contains the same amount of catabolic proteins and ribosomes as in the final state. During this second phase, the proteome gradually adapts due to growth-mediated dilution of inherited proteins. **c, f**, The growth rate almost fully adapts during the first phase (from  $t = 0$  to the circle) for the downshifts (green, cyan), but not for the upshifts (orange, purple). This difference is because of the high ribosome abundance in downshifts, which allows increased expression of catabolic proteins, and thus almost entirely avoids the slow phase, and is more prominent for shifts to fast final growth (**a–c**), than to slow final growth (**d–f**).





**Extended Data Figure 10 | Protein degradation.** **a**, Pulse-labelling allows the differentiation of pre-pulse and post-pulse protein mass. We added concentrated  $^{15}\text{NH}_4\text{Cl}$  into the culture at the moment of gluconate upshift or a few minutes before glucose exhaustion during the downshift. Comparing to a third isotope species (spiked-in  $^{15}\text{N}$ -reference culture) allows tracking the levels of pre-shift proteins over time. **b**, A schematic showing the levels of total cellular protein (black) and cellular protein existing at pulse time (blue) as the culture is instantaneously upshifted. Stable protein levels are characterized by a zero-slope line (blue solid line), whereas degrading or exported cellular proteins exhibit a negative-slope line (blue dashed line, red arrow). **c**, The post-shift levels of 40 cellular proteins of highest mass fraction were quantified using the pulse-labelling approach. Light (L,  $^{14}\text{N}$ ) over heavy (H,  $^{15}\text{N}$ ) relative

protein levels are plotted as a function of time. These proteins span diverse biological functions, cellular localization, size and structure. Together, they account for 35–40% of the total protein mass detected throughout the shift (estimated by summing their mass abundances listed in Supplementary Table 2 for each condition). With the exception of flagellin (fliC, red box), we did not observe decreasing protein levels for either the upshift or downshift series on the 2-h timescale for large-abundance proteins, which we could confidently quantify. Flagellin is exported to the cell periphery by a dedicated transport system, and probably shed into the medium during steady-state growth. As shed proteins are not collected at the same efficiency as proteins in cells, the decline of pre-labelled FliC serves as a positive control for the method.

## Life Sciences Reporting Summary

Nature Research wishes to improve the reproducibility of the work that we publish. This form is intended for publication with all accepted life science papers and provides structure for consistency and transparency in reporting. Every life science submission will use this form; some list items might not apply to an individual manuscript, but all fields must be completed for clarity.

For further information on the points included in this form, see [Reporting Life Sciences Research](#). For further information on Nature Research policies, including our [data availability policy](#), see [Authors & Referees](#) and the [Editorial Policy Checklist](#).

## ▶ Experimental design

## 1. Sample size

Describe how sample size was determined.

Not applicable

## 2. Data exclusions

Describe any data exclusions.

In quantitative mass spectrometry data, we used all data to calculate the "absolute expression data". We excluded proteins for the analysis of "relative expression data" that could not be normalized due to a missing identification in the normalization samples. We further excluded proteins that were identified in fewer than 50% of the time-points in Fig. 3a. See Methods for details.

## 3. Replication

Describe whether the experimental findings were reliably reproduced.

Growth transition kinetics are highly reproducible, as shown in Extended Data Fig. 2.

## 4. Randomization

Describe how samples/organisms/participants were allocated into experimental groups.

Not applicable

## 5. Blinding

Describe whether the investigators were blinded to group allocation during data collection and/or analysis.

Not applicable

Note: all studies involving animals and/or human research participants must disclose whether blinding and randomization were used.

## 6. Statistical parameters

For all figures and tables that use statistical methods, confirm that the following items are present in relevant figure legends (or in the Methods section if additional space is needed).

n/a Confirmed

- The exact sample size ( $n$ ) for each experimental group/condition, given as a discrete number and unit of measurement (animals, litters, cultures, etc.)
- A description of how samples were collected, noting whether measurements were taken from distinct samples or whether the same sample was measured repeatedly
- A statement indicating how many times each experiment was replicated
- The statistical test(s) used and whether they are one- or two-sided (note: only common tests should be described solely by name; more complex techniques should be described in the Methods section)
- A description of any assumptions or corrections, such as an adjustment for multiple comparisons
- The test results (e.g.  $P$  values) given as exact values whenever possible and with confidence intervals noted
- A clear description of statistics including central tendency (e.g. median, mean) and variation (e.g. standard deviation, interquartile range)
- Clearly defined error bars

See the web collection on [statistics for biologists](#) for further resources and guidance.

## ► Software

Policy information about [availability of computer code](#)

### 7. Software

Describe the software used to analyze the data in this study.

For mass spectrometry processing, WIFF-format instrument data files were converted to profile and centroid MZML formats using Sciex software. Using the Trans-Proteomic Pipeline<sup>34</sup> centroided mzML files were converted to mzXML and searched using X!Tandem<sup>35</sup> against a custom E. coli database (derived from UniProt organism 83333). The MS2 search results were combined into raw and consensus spectral libraries using SpectraST. See Methods for details.

For manuscripts utilizing custom algorithms or software that are central to the paper but not yet described in the published literature, software must be made available to editors and reviewers upon request. We strongly encourage code deposition in a community repository (e.g. GitHub). *Nature Methods* [guidance for providing algorithms and software for publication](#) provides further information on this topic.

## ► Materials and reagents

Policy information about [availability of materials](#)

### 8. Materials availability

Indicate whether there are restrictions on availability of unique materials or if these materials are only available for distribution by a for-profit company.

No unique materials were used.

### 9. Antibodies

Describe the antibodies used and how they were validated for use in the system under study (i.e. assay and species).

Not applicable

### 10. Eukaryotic cell lines

a. State the source of each eukaryotic cell line used.

Not applicable

b. Describe the method of cell line authentication used.

Not applicable

c. Report whether the cell lines were tested for mycoplasma contamination.

Not applicable

d. If any of the cell lines used are listed in the database of commonly misidentified cell lines maintained by [ICLAC](#), provide a scientific rationale for their use.

Not applicable

## ► Animals and human research participants

Policy information about [studies involving animals](#); when reporting animal research, follow the [ARRIVE guidelines](#)

### 11. Description of research animals

Provide details on animals and/or animal-derived materials used in the study.

Not applicable

Policy information about [studies involving human research participants](#)

### 12. Description of human research participants

Describe the covariate-relevant population characteristics of the human research participants.

Not applicable